# Theoretical analysis of $\Lambda(1405) \to (\Sigma\pi)^0$ mass spectra produced in $p + p \to p + \Lambda(1405) + K^+$ reactions

Maryam Hassanvand[1,2], Seyed Zafarollah Kalantari[2], Yoshinori Akaishi[1,3], and Toshimitsu Yamazaki[1,4]
[1] *RIKEN, Nishina Center, Wako, Saitama 351-0198, Japan*
[2] *Department of Physics, Isfahan University of Technology, Isfahan 84156-83111, Iran*
[3] *College of Science and Technology, Nihon University, Funabashi, Chiba 274-8501, Japan and*
[4] *Department of Physics, University of Tokyo, Bunkyo-ku, Tokyo 113-0033, Japan*
(Dated: October 10, 2018; published in PRC 87, 055202 (2013) + Errata)

We formulated the $\Lambda(1405)$ (abbreviated as $\Lambda^*$) $\to (\Sigma\pi)^0$ invariant-mass spectra produced in $p + p \to p + \Lambda^* + K^+$ reactions, in which both the incident channel for a quasi bound $K^-p$ state and its decay process to $(\Sigma\pi)^0$ were taken into account realistically. We calculated $M(\Sigma\pi)$ spectral shapes for various theoretical models for $\Lambda^*$. These asymmetric and skewed shapes were then compared with recent experimental data of HADES, yielding $M(\Lambda^*) = 1405^{+11}_{-9}\,\mathrm{MeV}/c^2$ and $\Gamma = 62 \pm 10$ MeV, where the interference effects of the $\bar{K}N$-$\Sigma\pi$ resonance with the $I = 0$ and 1 $\Sigma\pi$ continuum are considered. The nearly isotropic proton distribution observed in DISTO and HADES is ascribed to a short collision length in the production of $\Lambda^*$, which justifies the high sticking mechanism of $\Lambda^*$ and the participating proton into $K^-pp$.

PACS numbers: 21.45.-v, 13.75.-n, 21.30.Fe, 21.90.+f

## I. INTRODUCTION

The $\Lambda(1405)$ resonance discovered in 1961 [1] (called herein $\Lambda^*$) has strangeness $S$ = -1, spin-parity $J^p = (\frac{1}{2})^-$ , and isospin $I = 0$. It has been interpreted as a quasi bound state of $K^-p$ embedded in the $\Sigma + \pi$ continuum since Dalitz-Tuan's original prediction [2]. In recent years, Akaishi *et al.* derived phenomenologically a complex $\bar{K}N$ interaction (called here the $AY$ interaction) [3–5] based on the mass and width of $\Lambda(1405)$, $M = 1405.1^{+1.3}_{-1.0}$ MeV/$c^2$ and $\Gamma = 50 \pm 2$ MeV [6–8], [the so-called $\Lambda(1405)$ ansatz]. They applied this very attractive interaction to few-nucleon systems involving one and two $\bar{K}$'s, and found nuclear bound states with unusually high nuclear density [3, 9–12]. On the other hand, a totally different framework with a double-pole structure of $\Lambda(1405)$ has emerged on the basis of chiral SU(3) dynamics (called here *Chiral*), on which $\Lambda(1405)$ is claimed to consist of two poles around 1420 and 1390 MeV/$c^2$, which are coupled mainly to $\bar{K}N$ and $\Sigma\pi$ channels, respectively [13, 14]. Then, the resulting weakly attractive $\bar{K}N$ interaction leads to much shallower $\bar{K}$ bound states [15, 16].

Thus, it is vitally important to determine the location of the $K^-p$ resonance, whether $\Lambda(1405)$ is located at 1405 MeV/$c^2$ or above 1420 MeV/$c^2$, from experimental data without prejudice. For this purpose we have to treat the $\Lambda(1405)$ structure with the $AY$ model and the *Chiral* model on equal footing to be compared with experimental data. To resolve this issue, observations of $M(\Sigma\pi)$ spectra associated with resonant formation of $\Lambda^*$ in the stopped-$K^-$ absorption in $^{3,4}$He [17], and also in $d$ [18] have been proposed. Whereas old bubble-chamber experiments of stopped $K^-$ in $^4$He [19] indicated a preference of $\Lambda(1405)$ over $\Lambda(1420)$ [8, 18], a much more precise experiment with a deuteron target is expected at J-PARC [20]. Alternatively, Jido *et al.* [21] proposed an in-flight $K^-$ reaction on $d$, whereas Miyagawa and Haidenbauer [22] questioned the effectiveness of this method. In any case, old data on the in-flight $K^- + d$ reaction by Braun *et al.* [23] had a large statistical uncertainty in distinguishing $\Lambda(1420)$ and $\Lambda(1405)$, according to our statistical analysis. Future experiments at J-PARC of both stopped-$K^-$ [20] and in-flight $K^-$ [24] on $d$ are expected to give a convincing conclusion.

Recent experiments on high-energy $pp$ collisions have produced important data on the production of $\Lambda(1405)$:

$$p + p \to p + \Lambda^* + K^+,$$
$$\Lambda^* \to \Sigma^{+,0,-} + \pi^{-,0,+}. \qquad \text{(I.1)}$$

The ANKE experiment at COSY with an incident kinetic energy ($T_p$) of 2.83 GeV by Zychor *et al.* [25] has yielded a $(\Sigma^0\pi^0)^0$ invariant-mass spectrum. It was analyzed by Geng and Oset [26] based on chiral SU(3) dynamics. They showed that the reaction in the $\Lambda^*$ production region is dominated by the $|T_{21}|^2 k_2$ process, and they claimed that the spectrum develops a pronounced strength around 1420 MeV/$c^2$, which differs from the 1405 MeV/$c^2$ peak in Hemingway's data [27] analyzed by the $|T_{22}|^2 k_2$ process [6, 7] (see also Akaishi *et al.* [28]). This result might have been accepted as evidence for a double-pole structure of $\Lambda^*$ predicted by chiral SU(3) dynamics [13, 14], if the statistics of the data were good enough. The ANKE data were also analyzed by Esmaili *et al.* [18], who, on the contrary, showed from a fair statistical comparison between the two models that the data were in more favor of the $AY$ model, but the statistical significance was not sufficient to conclusively distinguish between *Chiral* and $AY$ models. Thus, new data from HADES of GSI, which have just been published [29, 30], are valuable for solving the present controversy.

In the present paper we formulate the spectral shape of the $(\Sigma\pi)^0$ mass to provide theoretical guides to analyze experimental data of $(\Sigma\pi)^0$ mass spectra from the above reaction. We take into account both the formation and the decay processes of $\Lambda(1405)$ in $pp$ reactions realistically, following our $\bar{K}N-\Sigma\pi$ coupled-channel formalism [5]. In this way, we derive the general form of the spectral function, which is not symmetric, but skewed with respect to the pole position. Then, we analyze $(\Sigma^{+-}\pi^{-+})^0$ spectra from HADES at $T_p = 3.50$ GeV [30].

## II. FORMULATION

### A. Coupled-channel treatment of $\Lambda^*$

Our coupled-channel treatment of $\Lambda(1405)$ is described in [5, 18]. We employ a set of separable potentials with a Yukawa-type form factor,

$$\langle \vec{k}_i'|v_{ij}|\vec{k}_j\rangle = g(\vec{k}_i')\,U_{ij}\,g(\vec{k}_j), \qquad \text{(II.2)}$$

$$g(\vec{k}) = \frac{\Lambda^2}{\Lambda^2+\vec{k}^2}, \qquad \text{(II.3)}$$

$$U_{ij} = \frac{1}{\pi^2}\frac{\hbar^2}{2\sqrt{\mu_i\mu_j}}\frac{1}{\Lambda}s_{ij}, \qquad \text{(II.4)}$$

where $i$ ($j$) stands for the $\bar{K}N$ channel, 1, or the $\pi\Sigma$ channel, 2, and $\mu_i$ ($\mu_j$) is the reduced mass of channel $i$ ($j$). Two of the non-dimensional strength parameters, $s_{11}$ and $s_{12}$, with a fixed $s_{22}$ are adjusted so as to reproduce a set of assumed $M$ and $\Gamma$ values for the $\Lambda^*$ pole [5]. The transition matrices,

$$\langle \vec{k}_i'|t_{ij}|\vec{k}_j\rangle = g(\vec{k}_i')\,T_{ij}\,g(\vec{k}_j), \qquad \text{(II.5)}$$

satisfy

$$T_{ij} = U_{ij} + \sum_l U_{il}\,G_l\,T_{lj}, \qquad \text{(II.6)}$$

$$G_l = \frac{2\mu_l}{\hbar^2}\int d\vec{q}\,g(\vec{q})\,\frac{1}{k_l^2-q^2+i\epsilon}\,g(\vec{q}). \qquad \text{(II.7)}$$

The solution is given in a matrix form by

$$T = [1-UG]^{-1}U \qquad \text{(II.8)}$$

with

$$(UG)_{lj} = -s_{lj}\sqrt{\frac{\mu_j}{\mu_l}}\,\frac{\Lambda^2}{(\Lambda-i\,k_j)^2}, \qquad \text{(II.9)}$$

where $k_j$ is a relative momentum in channel $j$.

Among the matrix elements, $T_{11}$, $T_{12}$, $T_{21}$ and $T_{22}$, the experimentally observable quantities below the $\bar{K}+N$ threshold are $-(1/\pi)\,\mathrm{Im}\,T_{11}$, $|T_{21}|^2k_2$ and $|T_{22}|^2k_2$, where the second term with $g^2(k_2)\,g^2(k_1)$ is a $\Sigma\pi$ invariant-mass spectrum from the conversion process, $\bar{K}N\to\Sigma\pi$ (which we call the "$T_{21}$ invariant mass"). The $T_{21}$ invariant mass coincides with the $\bar{K}N$ missing-mass spectrum in the mass region below the $\bar{K}+N$ threshold, as denoted by relation [18], that

$$\mathrm{Im}\,T_{11} = |T_{21}|^2\,\mathrm{Im}\,G_2. \qquad \text{(II.10)}$$

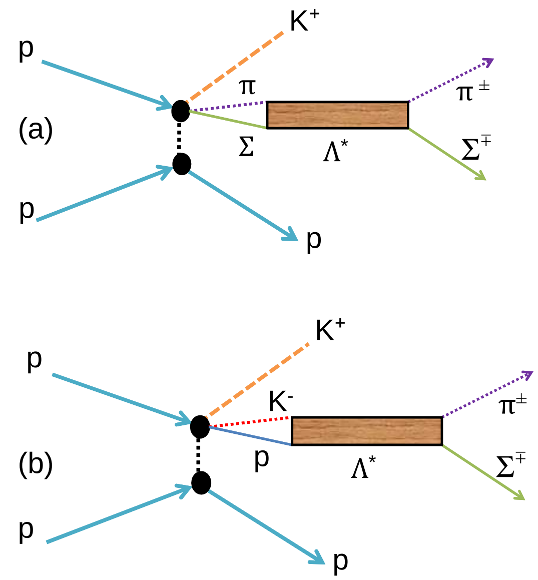


FIG. 1: (Color online) Feynman diagrams for the $p+p\to p+K^++\Lambda^*\to p+K^++(\Sigma\pi)^0$ reaction for (a) the process via $T_{22}$ and (b) the process via $T_{21}$.

The third term with $g^4(k_2)$ is a $\Sigma\pi$ invariant-mass spectrum from the scattering process, $\Sigma\pi\longrightarrow\Sigma\pi$ (which we call the "$T_{22}$ invariant mass").

### B. $\Lambda^*\to(\Sigma\pi)^0$ spectrum shape

The diagram for the reaction Eq. (I.1) is shown in Fig. 1. The decay processes via $T_{21}$ and $T_{22}$ are also given in this figure. The kinematical variables in the c.m. of the $pp$ collision for both the formation and the decay processes are given in Fig. 2.

In the present reaction we use $|T_{21}|^2k_2$ because the incident channel to bring $\Lambda(1405)$ is $K^-+p$ together with $K^+$ [see Fig. 1(b)]. This was also concluded by Geng and Oset [26], who studied the reaction mechanism in detail. The $|T_{22}|^2k_2$ spectrum would be applicable when $\Sigma$ and $\pi$ mesons are available in the incident channel, as shown in Fig. 1(a). The $|T_{22}|^2k_2$ spectrum is characterized by a large tail [18] in the higher-mass region up to the kinematical limit, which can in principle be recognizable by an observed spectrum. Experimentally, however, a bump in the upper-tail region may be masked by an ambiguous shape of the continuous background, and may thus be difficult to extract. We may allow a small admixture of $|T_{22}|^2k_2$ in our likelihood analysis of the experimental data.

The $|T_{21}|^2k_2$ and $|T_{22}|^2k_2$ curves of the *Chiral* model, as given by Hyodo and Weise [15] as well as those of the *AY* model, are shown in Fig. 1 (upper) of Ref. [18]. They will be compared with the new HADES data at the end of the present paper.

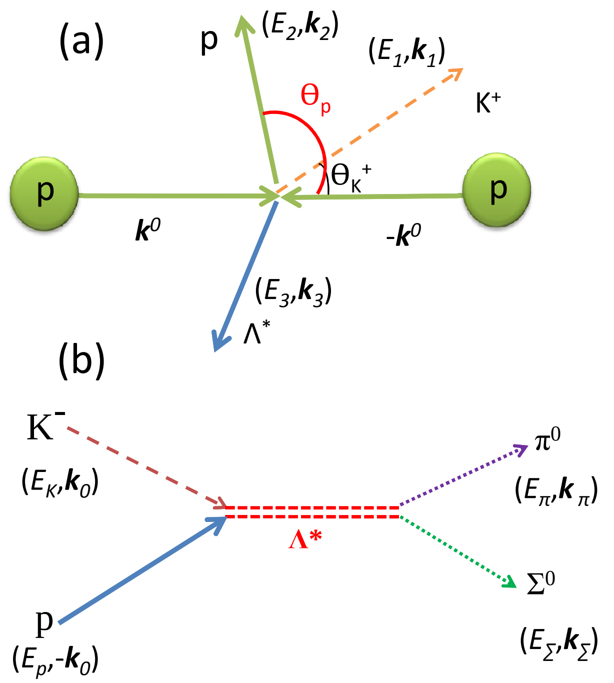


FIG. 2: (Color online) Kinematical variables in the center of mass of the $pp$ collision for (a) the formation process, $W_{\rm form}$, and (b) the decay channel, $G(x)$.

### C. Spectral function in the $pp$ reaction: $S(x)$

Now, we consider the spectrum function of the invariant mass, $S(x)$, in the case of $pp$ reactions. We compose it in the impulse approximation framework by using the incident channel function, $W_{\rm form}(x)$, and the decay channel one, $G(x)$, as follows:

$$S(x) = W_{\rm form}(x) \times G(x), \tag{II.11}$$

with

$$x = M(\Sigma\pi). \tag{II.12}$$

$G(x)$ is expressed in terms of the $T$ matrices, $T_{22}$ and $T_{21}$, as shown in Figs. 1-(a) and 1-(b). Each function calculated for an assumed $M$ of the $\Lambda^*$ pole is shown in Fig. 3.

### D. Formation process function: $W_{\rm form}$

The $\Lambda^*$ formation from $pp$ collision is calculated in a similar way as was done in [4]. We apply an impulse approximation to the formation process of Fig. 1 with a model impulse $t$ matrix,

$$\langle \vec{r}_{\Lambda^*-p}, \vec{r}_{(\Lambda^* p)-K^+} | t | \vec{r}_{p-p} \rangle$$
$$= T_0 \; \delta(\vec{r}_{\Lambda^*-K^+}) \int d\vec{r} \; \frac{\exp(-r/b)}{b^2 r} \delta(\vec{r}_{\Lambda^*-p} - \vec{r}) \delta(\vec{r}_{p-p} - \vec{r}), \tag{II.13}$$

where $\vec{r}_{a-b} = \vec{r}_a - \vec{r}_b$, $T_0$ is a strength parameter, and $b = m_B c/\hbar$ is a range which affects the dependence of the reaction amplitude on the momentum transfer to the adjacent proton in the $pp \to K^+\Lambda^* p$ process. Then, the $\Lambda^*$ formation probability is given as follows:

$$W_{\rm form}(x) = \frac{2\left|T_0\right|^2}{(2\pi)^3(\hbar c)^6} \frac{E_0}{k_0}$$
$$\times \int dE_1 \int d\Omega_1 \, d\Omega_2 \left(\frac{1}{1+b^2Q^2}\right)^2$$
$$\times \, k_1 k_2 E_1 E_2 \left[1 + \frac{E_2}{E_3}\left(1 + \frac{k_1}{k_2}\cos\theta_{pK^+}\right)\right]^{-1} \tag{II.14}$$

where $E_0$ and $k_0$ are the initial energy and momentum in the c.m. frame, as given by

$$k_0 = \frac{1}{\hbar} \left[\frac{1}{2} M_p \, T_p\right]^{\frac{1}{2}}. \tag{II.15}$$

The other quantities, $k_2, E_2$, and $E_3$, become functions of $x$ due to conservation of momentum and energy, which is applied to all the participating particles to take recoil effects into account. Also, $\theta_{pK^+} = (\theta_p - \theta_{K^+})$ is the angle between $K^+$ and $p$, $b$ is the range of the $pp$ reaction, and the momentum transfer, $Q$, is

$$Q = [{k_0}^2 + {k_2}^2 - 2\, k_0 \, k_2 \cos\theta_{\rm p}]^{\frac{1}{2}}. \tag{II.16}$$

As can be seen from the factor, $1/(1 + b^2Q^2)^2$, a shorter range of $b$ can effectively moderate the strong suppression due to a large momentum transfer, $Q$, in a high-energy $pp$ collision.

Figure 3(b) shows the behavior of $W_{\rm form}(x)$ for $T_p$ = 2.50, 2.83, and 3.50 GeV, the curves of which are normalized at $x = 1400$ MeV/$c^2$. They have respective kinematical upper limits, which make the mass distribution damp toward the kinematical limit. As a result, the observed spectrum shape, $S(x)$, changes, as demonstrated in Fig. 3(a), whereas $G(x)$ is independent of $T_p$.

### E. Decay process function: $G(x)$

The decay rate of $\Lambda(1405)$ to $(\Sigma\pi)^0$ is calculated by taking into account the emitted $\Sigma$ and $\pi$ particles realistically, following the generalized optical potential formalism in Feshbach theory [31], given by Akaishi *et al.* [5, 28]. The decay function, $G(x)$, is not simply a Lorentzian, but is skewed because the kinematic freedom of the decay particles is limited, particularly, when the

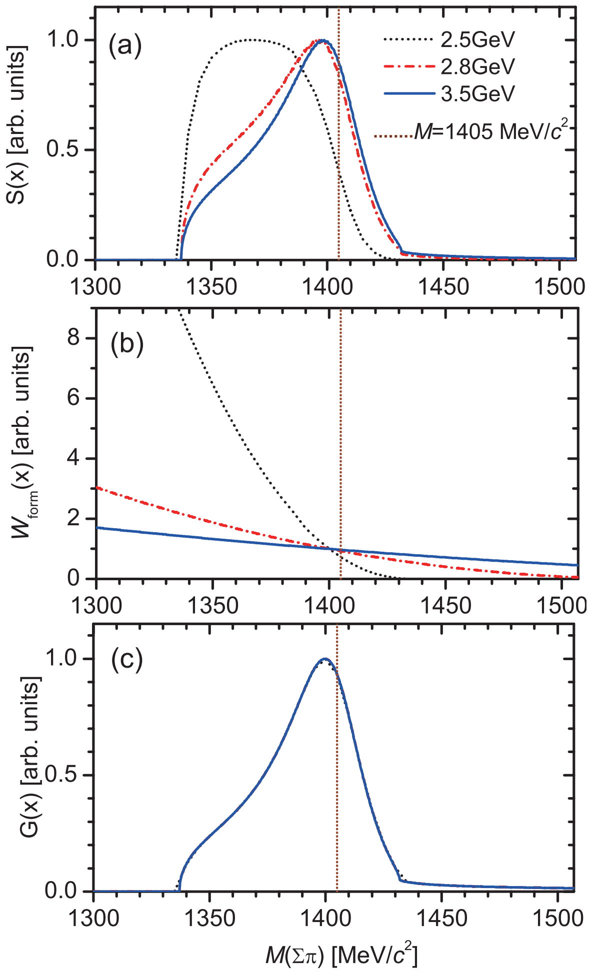


FIG. 3: (Color online) Normalized spectral functions $S(x)$ (a) composed of the formation-process function $W_{\rm form}$ (b) and the decay-process function $G(x)$ (c) for $T_p$ = 2.50, 2.85 and 3.50 GeV. $m_B$ = 770 MeV/$c^2$ and $(\theta_p, \theta_{pK+}) = (90^\circ, 180^\circ)$. The $M$ value of $\Lambda^*$ is assumed to be 1405 MeV/$c^2$, as indicated by the vertical dashed line.

incident proton energy, $T_p$, decreases and approaches the production threshold. Its general form is given as

$$G(x) = \frac{2(2\pi)^5}{\hbar^2 c^2} \frac{E_\pi E_\Sigma}{E_\pi + E_\Sigma} \,\mathrm{Re}\,[\tilde{k}(x)] \times \left|\langle \tilde{k}(x) | t | \tilde{k_0}(x) \rangle\right|^2, \tag{II.17}$$

where the relative momenta in the entrance and exit channels of Fig. 2(b) are calculated by

$$\tilde{k_0}(x) = \frac{c\sqrt{\lambda(x, m_K, M_p)}}{2\,\hbar\, x} \tag{II.18}$$

and

$$\tilde{k}(x) = \frac{c\sqrt{\lambda(x, m_\pi, M_\Sigma)}}{2\,\hbar\, x} \tag{II.19}$$

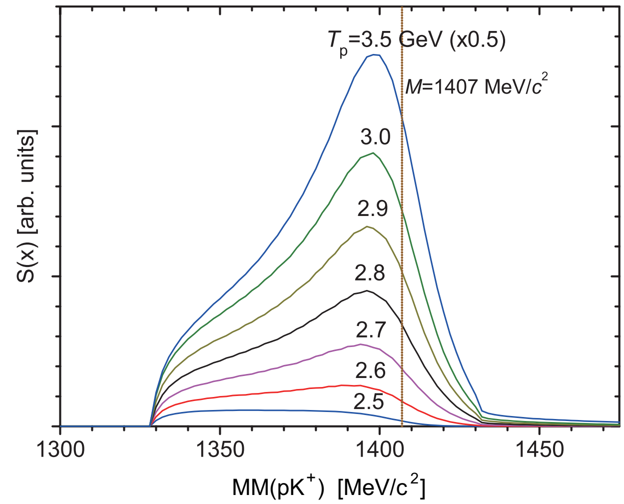


FIG. 4: (Color online) Incident energy dependence of the absolute values of the spectral function at $m_B$ = 770 MeV/$c^2$ and $(\theta_p, \theta_{pK+}) = (90^\circ, 180^\circ)$.

with

$$\lambda(x, m_1, m_2) \equiv (x + m_1 + m_2)(x + m_1 - m_2) \times (x - m_1 + m_2)(x - m_1 - m_2). \tag{II.20}$$

It should be noticed that $\lambda(x, m_K, M_p)$ becomes negative at around $x$ = 1400 MeV/$c^2$, where we must choose a positive Im $\tilde{k}$ on the physical Riemann sheet. This case corresponds to direct excitation of the $\Lambda^*$ quasi bound state from the $pp$ channel.

In the case of $AY$, the $T$ matrix is

$$\langle \tilde{k} | t_{21} | \tilde{k_0} \rangle = g(\tilde{k})\, T_{21}\, g(\tilde{k_0}) \tag{II.21}$$

for the $T_{21}$ process, and

$$g(\tilde{k}) = \frac{\Lambda^2}{\Lambda^2 + \tilde{k}^2} \tag{II.22}$$

with $\Lambda = m'_B c/\hbar$, $m'_B$ being the mass of an exchanged boson, and $\tilde{k}$ is the relative momentum of $\Sigma$ and $\pi$.

The shape of $G(x)$, as given by Eq.(II.17), includes the momenta $\tilde{k_0}$ and $\tilde{k}$, which are functions of $T_p$. However, the function $G(x)$ is shown to depend only on the invariant-mass $x$; namely, $G(x)$ is a unique function of $x$ and does not depend on $T_p$. It is bounded by the lower end ($M_l = M_\Sigma + m_\pi$ = 1328 MeV/$c^2$) and the upper end ($M_u = M_p + m_{K^-}$ = 1432 MeV/$c^2$).

It is to be noted that the position of the peak in $G(x)$ is significantly lower than the position of the pole ($M$ = 1405 MeV/$c^2$) in $T_{21}$, as assumed here and indicated by the vertical dashed line. Furthermore, the position of the peak (or centroid) of $S(x)$ is lowered due to the formation channel function $W_{\rm form}(x)$.

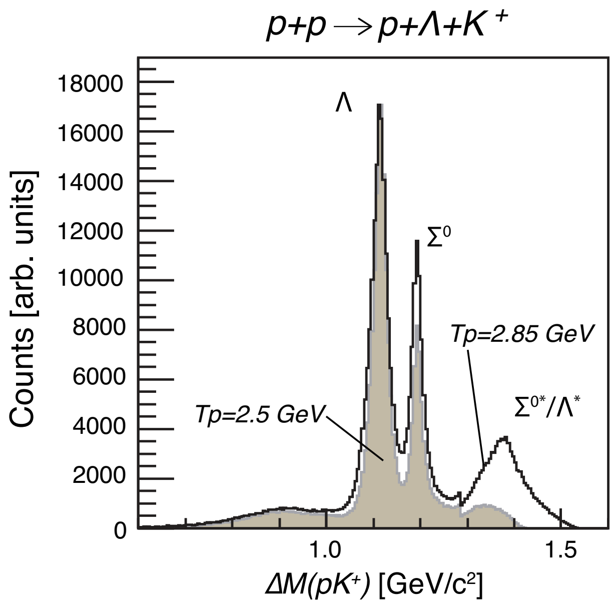


FIG. 5: (Color online) Experimental spectra of $\Delta M(pK^+)$ in the $pp \to p\Lambda K^+$ reaction at $T_p = 2.50$ and 2.85 GeV in DISTO experiments. Taken from [33].

## III. NUMERICAL RESULTS

In this section we present results from numerical calculations, and we discuss their physical implications. The importance of the present work is to consider both $W_{\rm form}(x)$ and $G(x)$ functions. In most illustrative samples, we applied the *AY* model with the Particle Data Group (PDG) parameters of [7], $M = 1407$ MeV$/c^2$ and $\Gamma = 50$ MeV. To compare the *Chiral* model with the *AY* model on equal footing, we also applied the same procedure as above to Hyodo-Weise's $T$ matrices to obtain realistic spectrum shapes $S(x)$.

### A. Dependence on the incident energy, $T_p$

For Eqs. (II.11), (II.14), and (II.17) again, it is clear that the spectral function depends on the incident proton energy due to the $W_{\rm form}(x)$ function and $G(x)$. Figure 4 shows absolute values of spectral functions $S(x)$ for various incident energies ($T_p$) at $m_B = 770$ MeV$/c^2$ and $(\theta_p, \theta_{pK^+}) = (90°, 180°)$. The shape of $S(x)$ is nearly the same, but toward the reaction threshold ($T_p^{\rm thresh} = 2.42$ GeV) not only does the absolute value diminish, but also the spectral shape changes drastically, as shown in Fig. 3(a) for the normalized spectral functions at $T_p =$ 3.50, 2.83 and 2.50 GeV. The most extreme case is seen at $T_p = 2.50$ GeV, where the main part of $x > 1400$ MeV$/c^2$ is missing due to the kinematical constraint, and a very skewed component below 1400 MeV$/c^2$ appears.

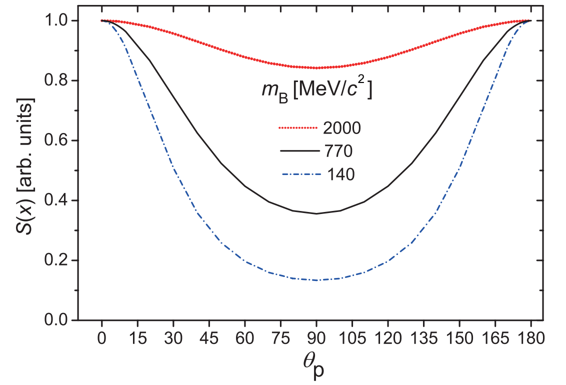


FIG. 6: (Color online) Normalized angular distributions of the outgoing proton for different exchanged boson masses, $m_B =$ 2000, 770 and 140 MeV$/c^2$, at $T_p = 3.50$GeV.

### B. Behavior near the production threshold of $T_p$

The above prediction is indeed in good agreement with the observed spectra of DISTO at $T_p = 2.50$ and 2.85 GeV [33], as shown in Fig. 5. Even in such a very skewed spectrum, one can extract the decay function, $G(x)$, from an observed spectral function by taking the ratio

$$\mathrm{DEV}[G(x)] \equiv \frac{S(x)^{\rm obs}}{W_{\rm form}(x)} \qquad \text{(III.23)}$$

using a calculated $W_{\rm form}$ function. This is a kind of the *deviation spectrum method* introduced in stopped-$K^-$ spectroscopy [18].

### C. Angular distribution and correlation

The cross section of this reaction has substantial angular dependence (Fig. 6), but the bound-state peak is distinct at any angle, and we can choose $(\theta_p, \theta_{pK^+}) =$ $(90°, 180°)$, because the cross section is modest and the peak-to-background ratio remains large. The normalized cross sections (spectral shapes) at various angles are found to be nearly the same. Since the two incident protons are indistinguishable, the $\Lambda(1405)$ formation process is angular symmetric, as shown in Fig. 6. We can write

$$\sigma(\theta_p, \theta_{pK^+}) = \sigma(\pi - \theta_p, -\theta_{pK^+}) \qquad \text{(III.24)}$$

for $\theta_p = 0° - 90°$ and $\theta_{pK^+} = 0° - 180°$.

According to Eq. (II.14) and Eq. (II.16), $W_{\rm form}$, and thus the spectral function, $S(x)$, are related to the outgoing proton angle, $\theta_p$, and the angle between the outgoing proton and $K^+$, $\theta_{pK^+}$, as shown in Fig. 7. Although these curves look different, the spectrum shape does not depend on the angle. We choose and use $\theta_p =$ $90°$, $\theta_{pK^+} = 180°$ in all of the following calculations.

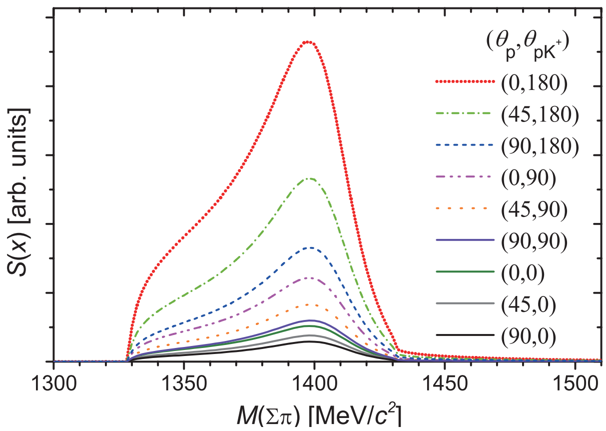


FIG. 7: (Color online) The spectral functions for various angles, ($\theta_p$, $\theta_{pK^+}$), for $T_p = 3.50$ GeV and $m_B = 770$ MeV/$c^2$.

### D. Dependence on the exchanged boson mass

Figure 6 shows the normalized angular distributions of the outgoing proton, $\theta_p$, for various masses of the exchanged boson, $m_B = 2000$, 770 and 140 MeV/$c^2$, at $T_p = 3.50$ GeV. The nearly isotropic angular distribution with a large boson mass explains the experimental data of HADES at $T_p = 3.50$ GeV [29, 30], which shows that the proton angular distributions together with $\Lambda(1405)$ and $\Lambda(1520)$ are nearly isotropic. A similar behavior is observed in the DISTO data at $T_p = 2.85$ GeV (see Fig. 5 of the present paper and Refs. [33, 34]). Such a short collision length as revealed in the production of $\Lambda(1405)$ in the $pp$ reaction is one of the key mechanisms ($\Lambda^*$ doorway) responsible for forming $K^-pp$ from high sticking of $\Lambda^*$ and $p$ [4]. On the other hand, it is well known that the proton emitted in the ordinary $pp \to p + \Lambda + K^+$ reaction has sharp forward and backward distributions, indicating that the mediating boson is $m_B = m_\pi$ [32–34].

## IV. $\chi^2$ FITTING OF HADES DATA

### A. HADES data

In this section we analyze the recent HADES data for charged final states of $\Sigma^-\pi^+$ and $\Sigma^+\pi^-$ in a $pp$ collision at $T_p = 3.50$ GeV. The data we use are the missing-mass spectra, $MM(pK^+)$, deduced by the HADES group, as given in Fig. 1 of [30], which are corrected for acceptance and efficiency of the detector system. They are expressed as

$$Y(x) = Y_{\Lambda^*}(x) + Y_{\Sigma^*}(x) + Y_{\Lambda 1520}(x) + Y_{\rm NonRes}(x), \tag{IV.25}$$

with $Y_{\Lambda^*}$ for $\Lambda^*$, $Y_{\Sigma^*}$ for $\Sigma(1385)$, $Y_{\Lambda 1520}$ for $\Lambda(1520)$, and $Y_{\rm NonRes}$ for the non resonant continuum. The HADES group decomposed the experimental data, $Y(x)$, by the above four components, which were obtained by model simulations, among which the $\Sigma(1385)$ and the $\Lambda(1520)$ components were determined by using the experimental data. The shape of the non-resonant $\Sigma\pi$ continuum was simulated. In their fitting they cautiously excluded the area around 1400 MeV/$c^2$ for $MM(pK^+)$ in order not to bias the finally extracted shape of the $\Lambda^*$ resonance. Then, they found that a simulation of the $\Lambda^*$ region by using a relativistic $s$-wave Breit-Wigner distribution with a width of 50 MeV/$c^2$ and a pole mass of 1385 MeV/$c^2$ can reproduce the experimental data very well, but using instead the nominal mass of 1405 MeV/$c^2$ fails.

This conclusion depends on their assumption of the symmetric Breit-Wigner shape, which is not valid in the case of a broad resonance with adjacent endpoints, $M(\Sigma + \pi)$ and $M(p + K^-)$, as we have seen. Thus, in turn, we decided to set up an excess component, $Y_{\Lambda^*}(x)$, by subtracting the given three components from the experimental spectrum $Y(x)$ as

$$Y_{\Lambda^*}(x) = Y(x) - Y_{\Sigma^*}(x) - Y_{\Lambda 1520}(x) - Y_{\rm NonRes}(x), \tag{IV.26}$$

where the statistical errors of $Y(x)$ are inherited to $Y_{\Lambda^*}(x)$.

### B. Interference effects between the $\bar{K}N$ resonance and the $\Sigma\pi$ continuum

Before going into the analysis of the HADES data we discuss possible interference effects between the $\bar{K}N$ resonance and the $\Sigma\pi$ continuum.

#### 1. *Interference with the $I = 1$ $\Sigma\pi$ continuum*

The charge-basis $T$ matrices are related to the isospin-basis $T$ matrices as

$$|T_{\Sigma^+\pi^-}|^2 \approx \frac{1}{3}|T_{I=0}|^2 + \frac{1}{2}|T_{I=1}|^2 + \sqrt{\frac{2}{3}}{\rm Re}[T^*_{I=0}T_{I=1}], \tag{IV.27}$$

$$|T_{\Sigma^-\pi^+}|^2 \approx \frac{1}{3}|T_{I=0}|^2 + \frac{1}{2}|T_{I=1}|^2 - \sqrt{\frac{2}{3}}{\rm Re}[T^*_{I=0}T_{I=1}], \tag{IV.28}$$

where $|T_{I=2}|^2$ is neglected. The HADES $\Sigma^+\pi^-$ and $\Sigma^-\pi^+$ data show similar behavior: the $\chi^2$ best-fit mass of each of the two spectra is obtained to be very close to one another. This means that the interference term between $I = 0$ and $I = 1$ has only a small effect on the resonance spectral shape. Then, we can treat the $I = 1$ contribution as a part of $Y_{\rm NonRes}$ in the analysis of the $I = 0$ $\Lambda^*$ resonance, disregarding the interference especially for the sum of the $\Sigma^+\pi^-$ and $\Sigma^-\pi^+$ data.

*2. Interference with $I = 0$ $\Sigma\pi$ continuum*

$\Lambda(1405)$ ( $= \Lambda^*$) is a $I = 0$ $L = 0$ $\bar{K}N$ resonance state coupled with the $I = 0$ $L = 0$ $\Sigma\pi$ continuum. Our theoretical spectrum curves in Fig. 11 already include the $\bar{K}N$ threshold effect and also the interference effect with the $I = 0$ $L = 0$ $\Sigma\pi$ continuum, because we have solved a $\bar{K}N$-$\Sigma\pi$ coupled-channel $T$-matrix equation. Thanks to the separation of $Y_{\rm NonRes}$ by the HADES group we need not calculate contributions from the $I = 0$ $L \geq 1$ $\Sigma\pi$ continuum and $I = 1$ all $L$ $\Sigma\pi$ continuum, which cause no interference to the $I = 0$ $L = 0$ $\Lambda^*$ resonance and therefore can be treated as $Y_{\rm NonRes}$: this is a great advantage of the HADES data for extracting the resonance-pole parameters, the mass and the width of $\Lambda^*$.

Now we estimate the effect of the $\bar{K}N$ threshold and the effect of interference with the $I = 0$ $L = 0$ $\Sigma\pi$ continuum. By fixing the mass of $\Lambda^*$ to be 1405 MeV$/c^2$, we change AMY's interaction strengths, $s_{11}, s_{12} = s_{21}$, so as to reproduce a given width range of 10 - 70 MeV. The obtained mass spectra are discussed below.

Figure 8 shows the $\bar{K}N$ threshold effect on the $\Sigma\pi$ invariant mass spectrum, $|t_{21}|^2 k_2$, where the interference effect is suppressed by putting $s_{22} = 0$. When the width is narrow enough, the spectrum is almost symmetric with a peak close to the pole position. When the width becomes wide, the peak position is lowered from the pole position and the spectrum shape is skewed: this is the $\bar{K}N$ threshold effect on the spectrum. Figure 9 shows results when the interference effect with the $I = 0$ $L = 0$ $\Sigma\pi$ continuum is switched on. The interference effect is not so large for the transition mass spectrum, $|t_{21}|^2 k_2$, since the entrance channel to form $\Lambda^*$ has no $\Sigma\pi$ continuum component.

On the other hand, Fig. 10 shows results of the conventional mass spectrum, $|t_{22}|^2 k_2$, including the interference effect with the $I = 0$ $L = 0$ $\Sigma\pi$ continuum. The interference effect is rather large, since the entrance going to $\Lambda^*$ consists of just $\Sigma\pi$ continuum components, which make the resonance shape deform appreciably. The peak shift comes almost from the interference with the $I = 0$ $L = 0$ $\Sigma\pi$ continuum, as seen from an inflection at the pole position and a succeeding interference minimum (see Fig. 8(b) of [35]). The CLAS data [36] seem to be a case of $|t_{22}|^2\, k_2$ where the coupling with the $\Sigma\pi$ continuum becomes significant. The interference between $I = 0$ and $I = 1$ $\Sigma\pi$ amplitudes gives rise to a strong charge dependence of $\Sigma^+\pi^-$, $\Sigma^0\pi^0$, and $\Sigma^-\pi^+$ mass spectra.

The HADES data are well fitted with the transition mass spectrum, $|t_{21}|^2 k_2$, as seen from the resemblance between $\Gamma = 60$ or 50 MeV curves of Fig. 9 and (a) or (b) of Fig. 11. It is noted that the peak shift takes place mainly due to the $\bar{K}N$ threshold effect in this case.

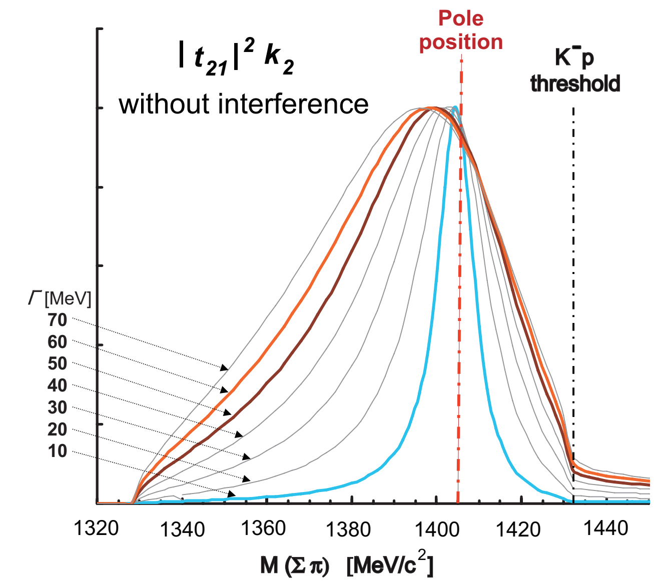


FIG. 8: Transition mass spectrum, $|t_{21}|^2 k_2$, including the $\bar{K}N$ threshold effect. All the heights are normalized to a same value.

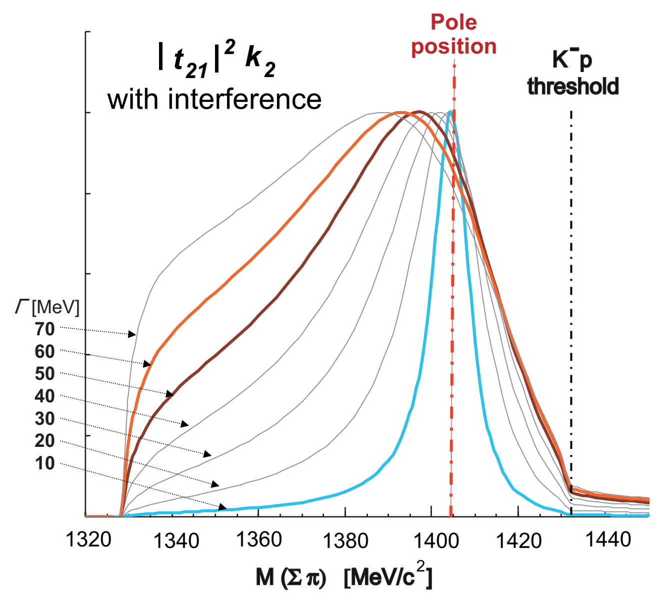


FIG. 9: Transition mass spectrum, $|t_{21}|^2 k_2$, including both the $\bar{K}N$ threshold effect and the interference effect with the $I = 0$ $L = 0$ $\Sigma\pi$ continuum. All the heights are normalized to a same value.

## C. Deduced mass and width

The HADES spectra, as given in Fig. 1 of [30], indicate that the spectra of the two charged channels are similar to each other, yielding nearly the same $M$ values. This

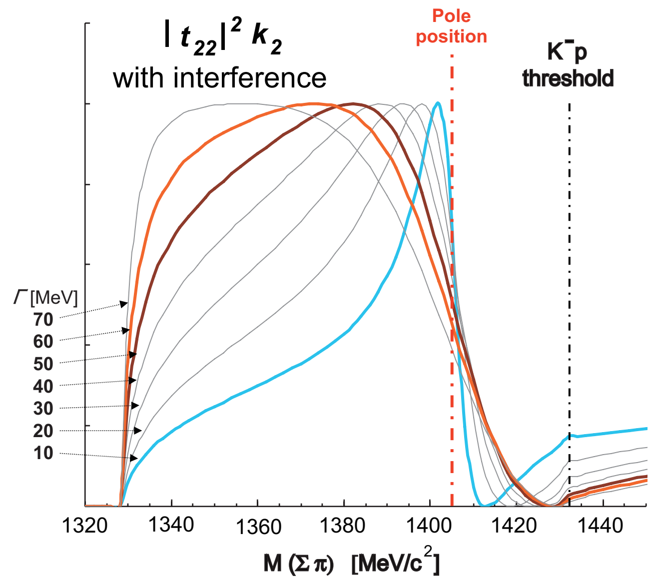


FIG. 10: Conventional mass spectrum, $|t_{22}|^2 k_2$, including both the $\bar{K}N$ threshold effect and the interference effect with the $I = 0$ $L = 0$ $\Sigma\pi$ continuum. All the heights are normalized to a same value.

fact indicates that the $\Sigma\pi$ resonance is formed by nearly pure charged states, $\Sigma^+\pi^-$ and $\Sigma^-\pi^+$, without isospin mixing. It also justifies the use of $T_{21}$ for the analysis of $M(\Sigma\pi)$ in the case of $pp$ reactions. On the other hand, the statistical fluctuation of each charged-channel spectrum is rather large. Thus, for the final analysis we use the sum data of HADES ($\Sigma^+\pi^- + \Sigma^-\pi^+$), which is presented in Fig. 1(c) of [30]. Keeping the last three components of Eq. (IV.26) fixed, we fit the experimental data of $Y_{\Lambda^*}(x)$ with $n = 21$ data points in the range of 1300 to 1550 MeV/$c^2$ (closed points with error bars in Fig. 11) by assumed theoretical functions $S(x)$.

Generally, the experimental histogram, $N_i$, $i = 1$, ..., $n$, with respective statistical errors, $\sigma_i$, is fitted to a theoretical curve, $S(x; M, \Gamma)$, with $x = MM(pK^+)$ involving the mass $M$ and width $\Gamma$ as free parameters by minimizing the $\chi^2$ value:

$$\chi^2(M, \Gamma) = \sum_{i=1}^{n} \left( \frac{N_i - S(x_i; M, \Gamma)}{\sigma_i} \right)^2 . \qquad \text{(IV.29)}$$

Figure 11 shows the results of the $\chi^2$ fitting, where the HADES data ($\Sigma^+\pi^- + \Sigma^-\pi^+$) at $T_p = 3.50$ GeV [30] are compared with best-fit theoretical spectral functions, $S(x)$. The present $AY$ treatment (hereafter called HKAY), with the PDG values ($M = 1405.1^{+1.3}_{-1.0}$ MeV/$c^2$ and $\Gamma = 50$ MeV [8]) adopted, gives a remarkable fitting with $\chi^2 = 11$, which is comparable with the statistically expected value, $< \chi^2 >_{\rm exp} \sim 19$. On the other hand, the *Chiral* model gives much larger $\chi^2$ values of $\sim$111, when $T_{21}$ is chosen, and of 39, when $T_{22}$ is chosen. Another *Chiral* model spectrum by Geng and Oset [26] is almost identical to HW's $T_{21}$. Thus, the chiral models indicate a substantial deviation from the experimental data.

Furthermore, we can find best-fit values of $(M, \Gamma)$ from drawing confidence contour curves by varying the parameters $(M, \Gamma)$ in a plane. The results are shown in Fig. 12. From this contour mapping we obtain the following best-fit values with 68% confidence levels ($1\sigma$) errors:

$$M = 1405^{+11}_{-9} \text{ MeV}/c^2, \qquad \text{(IV.30)}$$

$$\Gamma = 62 \pm 10 \text{ MeV}. \qquad \text{(IV.31)}$$

The best-fit curves are shown together with the experimental points in Fig. 11. The $M$ value thus obtained from the present analysis of the new HADES data confirms the traditional value [7, 8].

## V. CONCLUDING REMARKS

We have presented results of our calculation for the spectral shape of $MM(pK^+)$ in the $pp \to p\Lambda^* K^+$ reaction based on the $\bar{K}N$-$\Sigma\pi$ coupled-channel treatment. We took into account both the entrance process and the decay process. The formation probability, $W_{\rm form}$, of $\Lambda^*$ in a $pp$ collision and the decay rate, $G(x)$, to $(\Sigma\pi)^0$ were formulated. The spectral function is given by $S(x) = W_{\rm form} \times G(x)$. It was found to be asymmetric and skewed due to the kinematic limitation imposed by the entrance channel. The peak of $S(x)$ is not located at the pole position.

With this tool in hand we analyzed the recent HADES data. The interference effects of the $\bar{K}N$-$\Sigma\pi$ resonance with $I = 0$ and 1 $\Sigma\pi$ continuum are considered. Although the observed spectra of $MM(pK^+)$ appear to show the peak position at around 1385 MeV/$c^2$, the $\chi^2$ fitting by our theoretical spectral functions provided $M = 1405^{+11}_{-9}$ MeV/$c^2$. This value is in good agreement with the values obtained from a recent analysis [17] of an old experimental data of stopped-$K^-$ in $^4$He [19], taken up as the updated PDG value ($M = 1405.1^{+1.3}_{-1.0}$ MeV/$c^2$) [8]. On the other hand, the *Chiral* model with $M \sim 1420$ MeV/$c^2$ cannot reproduce the experimental data.

The Faddeev method is suitable for treating final-state interactions of three particles. However, it is difficult to apply this method to the present high-energy $p$-induced processes where so many partial waves are involved. On the other hand, for the low-energy $K^- + d$ reaction Révai [37] succeeded in extracting the $\Lambda(1405)$ resonance structure by using the Faddeev method. We are considering an analysis future data of stopped $K^-$ on $d$, proposed in [18, 20], by fully taking account of final-state interactions in the Faddeev formalism.

The proton angular distribution in $\Lambda^*$ production was also calculated. The isotropic distribution observed in HADES [30] and DISTO [33, 34] were explained by a short-range collision with an intermediate boson mass heavier than the $\rho$ meson mass. This is consistent with the calculated large cross section for the production

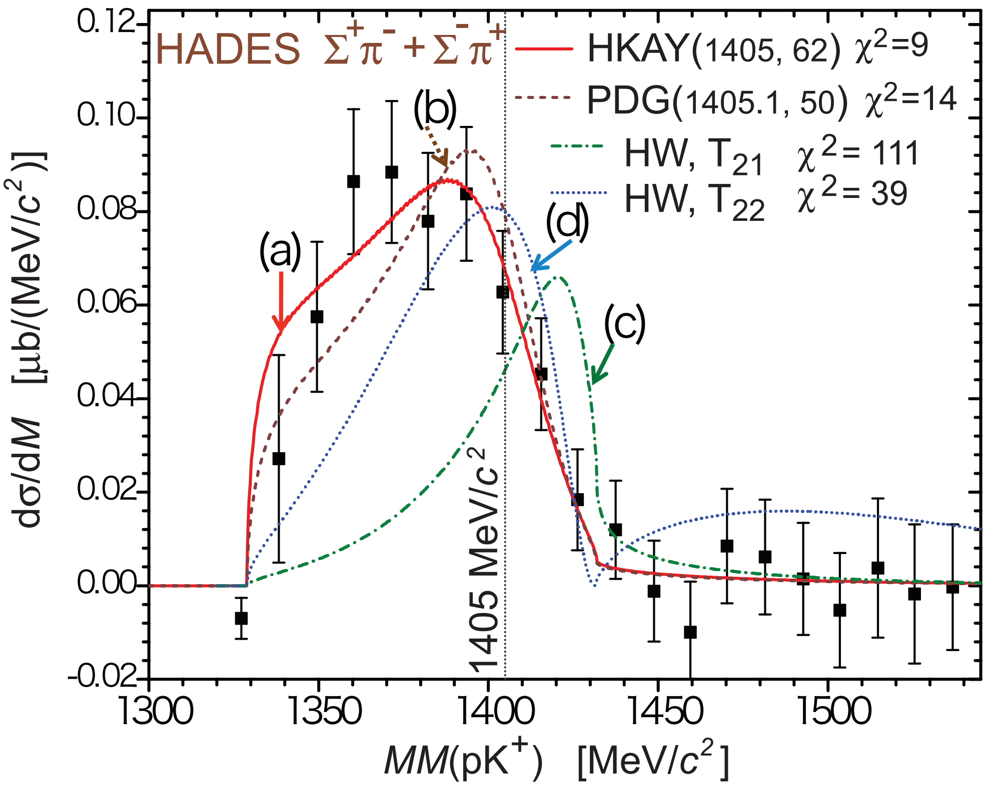


FIG. 11: (Color online) Comparison of HADES data ($\Sigma^+\pi^- + \Sigma^-\pi^+$, closed squares) at $T_p$ = 3.50 GeV [30] with best-fit theoretical spectral functions $S(x)$. (a) Best-fit HKAY curves (with $\chi^2 = 9.5$, $M = 1405^{+11}_{-9}$ MeV/$c^2$, and $\Gamma = 62 \pm 10$ MeV). (b) *AY* model with the PDG parameters (with $\chi^2 = 14$, $M = 1405.1^{+1.3}_{-1.0}$ MeV/$c^2$, and $\Gamma = 50$ MeV [8]). The *Chiral* model using HW's $T_{21}$ [with $\chi^2 = 111$, (c)] and $T_{22}$ [with $\chi^2 = 40$, (d)].

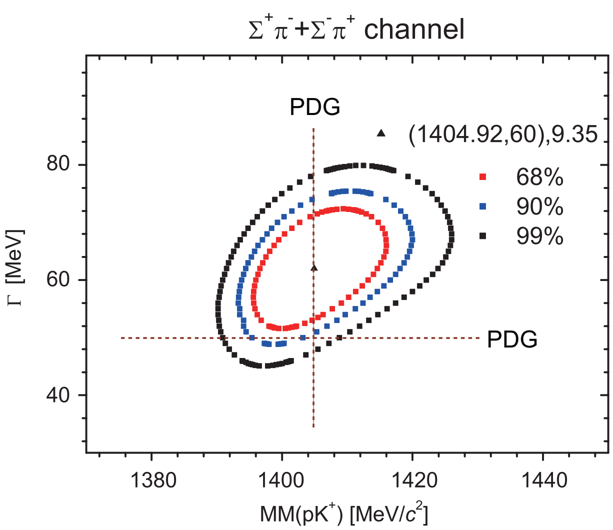


FIG. 12: (Color online) Confidence level contours from $\chi^2$ fitting of the HADES data of $\Sigma^+\pi^- + \Sigma^-\pi^+$ at $T_p$ = 3.50 GeV. The PDG values are also shown.

of $K^-pp$ in $pp$ collisions [4], which has recently been observed in DISTO experiments [32].

## VI. ACKNOWLEDGMENTS

This work is supported by a Grant-in-Aid for Scientific Research from the Ministry of Science, Research, and Technology of Iran and by a Grant-in-Aid for Scientific Research from Monbu kagakusho of Japan. One of us (T Y) acknowledges support by the Alexander von Humboldt Foundation, Germany.

[1] M.H. Alston *et al.*, Phys. Rev. Lett. **6**, 698 (1961).

[2] R.H. Dalitz and S.F. Tuan, Ann. Phys. (NY) **8**, 100

(1959).
[3] Y. Akaishi and T. Yamazaki, Phys. Rev. **C 65**, 044005 (2002).
[4] T. Yamazaki and Y. Akaishi, Phys. Rev. **76**, 045201 (2007).
[5] Y. Akaishi, K. S. Myint and T. Yamazaki, Proc. Jpn. Acad. **B 84**, 264 (2008); https://www.jstage.jst.go.jp/browse/pjab/
[6] R.H. Dalitz and A. Deloff, J. Phys. G: Nucl. Part. Phys. **17**, 289 (1991).
[7] K. Nakamura *et al.*, (Particle Data Group), J. Phys. **G 37**, 075021 (2010).
[8] J. Beringer *et al.*, (Particle Data Group), Phys. Rev. **D 86**, 010001 (2012).
[9] T. Yamazaki and Y. Akaishi, Phys. Lett. **B 535**, 70 (2002).
[10] A. Doté, H. Horiuchi, Y. Akaishi and T. Yamazaki, Phys. Lett. **B 590**, 51 (2004).
[11] A. Doté, H. Horiuchi, Y. Akaishi and T. Yamazaki, Phys. Rev. **C 70**, 044313 (2004).
[12] T. Yamazaki, A. Doté, and Y. Akaishi, Phys. Lett. **B 587**, 167 (2004).
[13] D. Jido, J.A. Oller, E. Oset, A. Ramos and U.G. Meissner, Nucl. Phys. **A 725**, 181 (2003).
[14] V. K. Magas, E. Oset and A. Ramos, Phys. Rev. Lett. **95**, 052301 (2005).
[15] T. Hyodo and W. Weise, Phys. Rev. **C 77**, 035204 (2008).
[16] A. Doté, T. Hyodo, and W. Weise, Phys. Rev. **C 79**, 014003 (2009).
[17] J. Esmaili, Y. Akaishi and T. Yamazaki, Phys. Lett. **B 686**, 23 (2010).
[18] J. Esmaili, Y. Akaishi and T. Yamazaki, Phys. Rev. **C 83**, 055207 (2011).
[19] B. Riley, I-T. Wang, J.G. Fetkovich and J.M. McKenzie, Phys. Rev. **D 11**, 3065 (1975).
[20] T. Suzuki, J. Esmaili and Y. Akaishi, EPJ Web Conf. **3**, 07014 (2010).
[21] D. Jido, E. Oset and T. Sekihara, Eur. Phys. J. **A 42**, 257 (2009).
[22] K. Miyagawa and J. Haidenbauer, Phys. Rev. **C 85**, 065201 (2012).
[23] O. Braun *et al.*, Nucl. Phys. **B 129**, 1 (1977).
[24] J-PARC E31 experiment; http://j-parc-jp/NuclPart/pac 0907/pdf/Noumi.pdf..
[25] I. Zychor *et al.*, Phys. Lett. **B 660**, 167 (2008).
[26] L. S. Geng and E. Oset, Eur. Phys. J. **A 34**, 405 (2007).
[27] R.J. Hemingway, Nucl Phys. **B 253**, 742 (1985).
[28] Y. Akaishi, T. Yamazaki, M. Obu, and M. Wada, Nucl., Phys. **A 835**, 67 (2010).
[29] G. Agakishiev *et al.* (HADES Collaboration), Phys. Rev. **C 85**, 035203 (2012).
[30] G. Agakishiev *et al.* (HADES Collaboration), Phys. Rev. **C 87**, 025201 (2013).
[31] H. Feshbach, Ann. Phys. (NY) **5**, 357 (1958); **19**, 287 (1962).
[32] T. Yamazaki *et al.*, Phys. Rev. Lett. **104**, 132502 (2010).
[33] P. Kienle *et al.*, Eur. Phys. J. A **48** (2012) 183.
[34] K. Suzuki *et al.* (private communication).
[35] O. Morimatsu and K. Yazaki, Nucl. Phys. **A 483**, 493 (1988).
[36] K. Moriya *et al.*, Phys. Rev. C **87**, 035206 (2013).
[37] J. Révai, arXiv:0635564 [nucl-th].